Supplementary materials for the manuscript "Significant Holocene hydrological evolution of subglacial Lake Snow Eagle, East Antarctica implied by englacial radio-stratigraphy"

AUTHORS: Shuai Yan, Michelle R. Koutnik, Donald D. Blankenship, Jamin S. Greenbaum, Duncan A. Young, Jason L Roberts, Tas van Ommen, Bo Sun, Martin J. Siegert

Supplementary Note #1, 2.5-D ice flow model

In this study, we combine the geophysical observation with a 2.5-D ice flow model to investigate the evolution of LSE. We build our model along the current ice-flow direction, measured by MEaSUREs InSAR-Based Antarctic Ice Velocity Map, Version 2 (Rignot and others, 2017). The first 70 kilometers of the flowline (near the ice divide) is difficult to confidently evaluate from satellite-derived ice surface velocity, because the flow rate near the ice divide is close to zero and within the measurement uncertainty. Therefore, for this part of the model domain near the ice divide, we had to build the model along a linear estimation of the flowline extending to the divide position, and where the orientation of this line was estimated from the overall ice-flow direction in the area. The ice flow near LSE is mostly in the grid north direction, and the radar survey profiles were designed to be aligned in this direction. Therefore, for the portion of the model domain near LSE that coincides with the radar sounding profile, we choose to use the radar profile as an approximated flowline. While there are small-scale deviations between the radar profile and the actual ice flow line, using the radar transect as a flowline allows us to directly extract englacial stratigraphy from radar sounding measurements. The alternative approach, which would require interpolating between transects, could introduce significant uncertainty due to our limited understanding of the exact 3-D shape of the isochron planes.

The ice-surface elevation in the downstream portion of the model domain (near LSE) is measured from radar sounding and is used as an initial condition for our steady-state ice-surface calculation, which is used to initiate the time-varying ice-surface calculation for layer modeling. The measured surface profile shows surface roughness at the scale of meters to tens of meters and changes in surface

slope that can introduce changes in elevation of up to 80 meters over a few kilometers near LSE.

We acknowledge that heat flux in Antarctica is not well constrained, where continent-scale heat flux products can vary significantly (e.g., Burton-Johnson and others, 2020; Kang and others, 2022). The estimate published in Maule and others (2005) was chosen in this study because the lower overall value made it possible to best approximate the observed ice surface given a prescribed surface temperature and accumulation distribution (Fig. S8). While it is true that we do not know the air temperature distribution and accumulation distribution very well, which includes any temporal variations in these values, we treat these as our best estimates and not as tunable parameters. There may be a different combination of parameter values that represent the observed surface using a higher heat flux estimate, but exploring those options was not a goal of this study as this would involve evaluating different reconstructions of poorly constrained air temperature and accumulation rate. The surface topography on the tens to hundreds of kilometers spatial scale is a constraint on the large-scale dynamic state, but the parameters involved in representing this in a simplified model are not necessarily unique. Given the focus of this study on other poorly constrained parameter values, we found that using Maule and others (2005) heat-flux estimate in combination with our estimates for air temperature and accumulation rate gave a reasonable representation of the observed ice surface (and also of the poorly known ice-surface velocity) (Fig. S8), so we used this as a framework in our modeling. The estimate of heat flux and the estimate of average surface temperature, and as a function of local ice thickness, are used to estimate a 1-D temperature profile at each horizontal grid point in the domain that defines the 2-D temperature field used in the model. The model is not thermomechanical coupled, so the ice temperature does not change over time in the model.

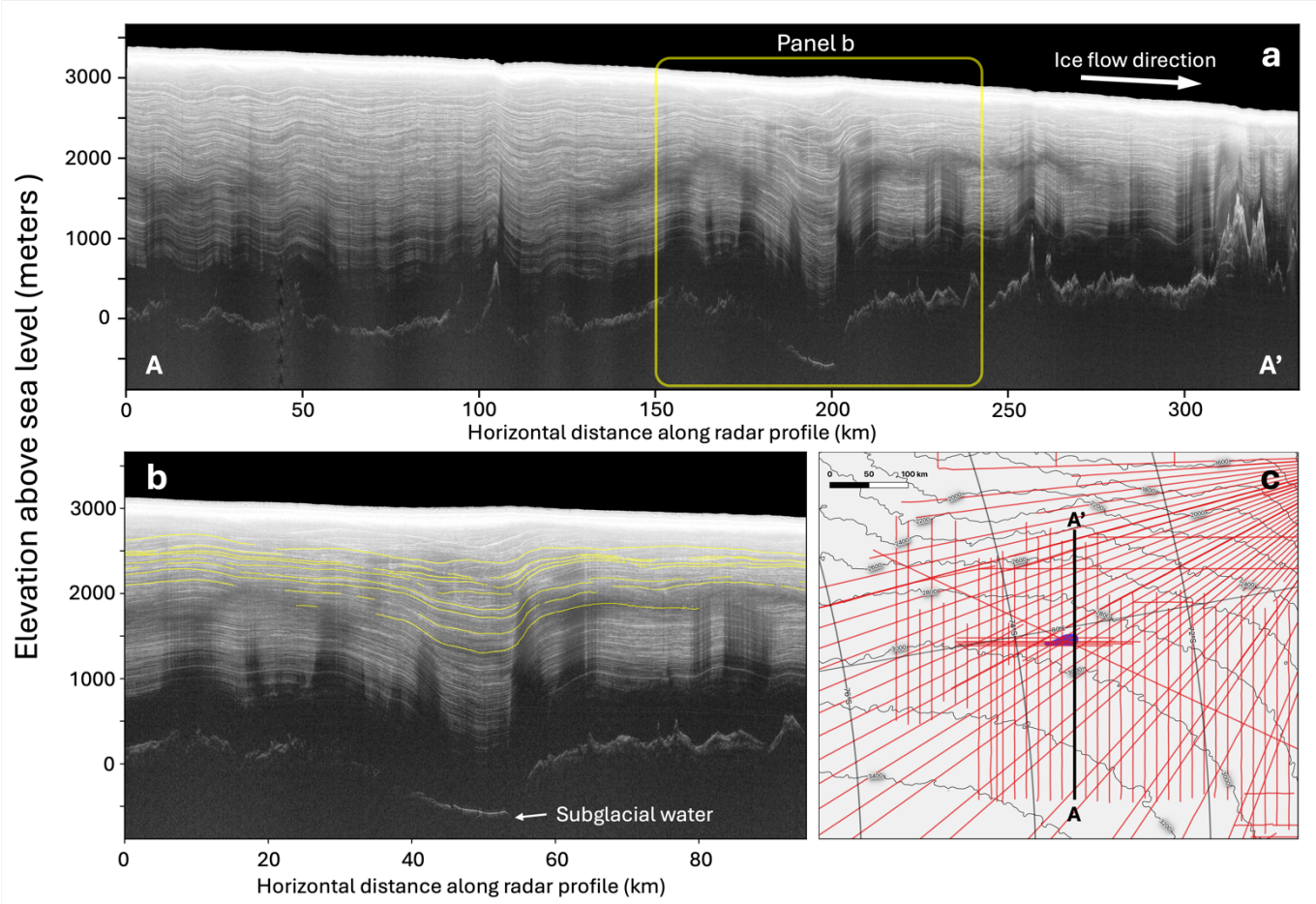

Fig. S1. Englacial radio-stratigraphy above LSE. a: Example radargram collected through the LSE area. The location and orientation of this radargram is marked in panel c. b: A zoom-in view of the anomalous stratigraphy above LSE, whose location is marked in panel(a. Yellow lines show the nine traced englacial reflections in the LSE area, with PEL_EDC_IRH01 being the shallowest (closest to the ice surface) and PEL_EDC_IRH09 being the deepest. c: Location and orientation of the radargram shown in panel a with respect to LSE (blue area) and other survey profiles (red lines).

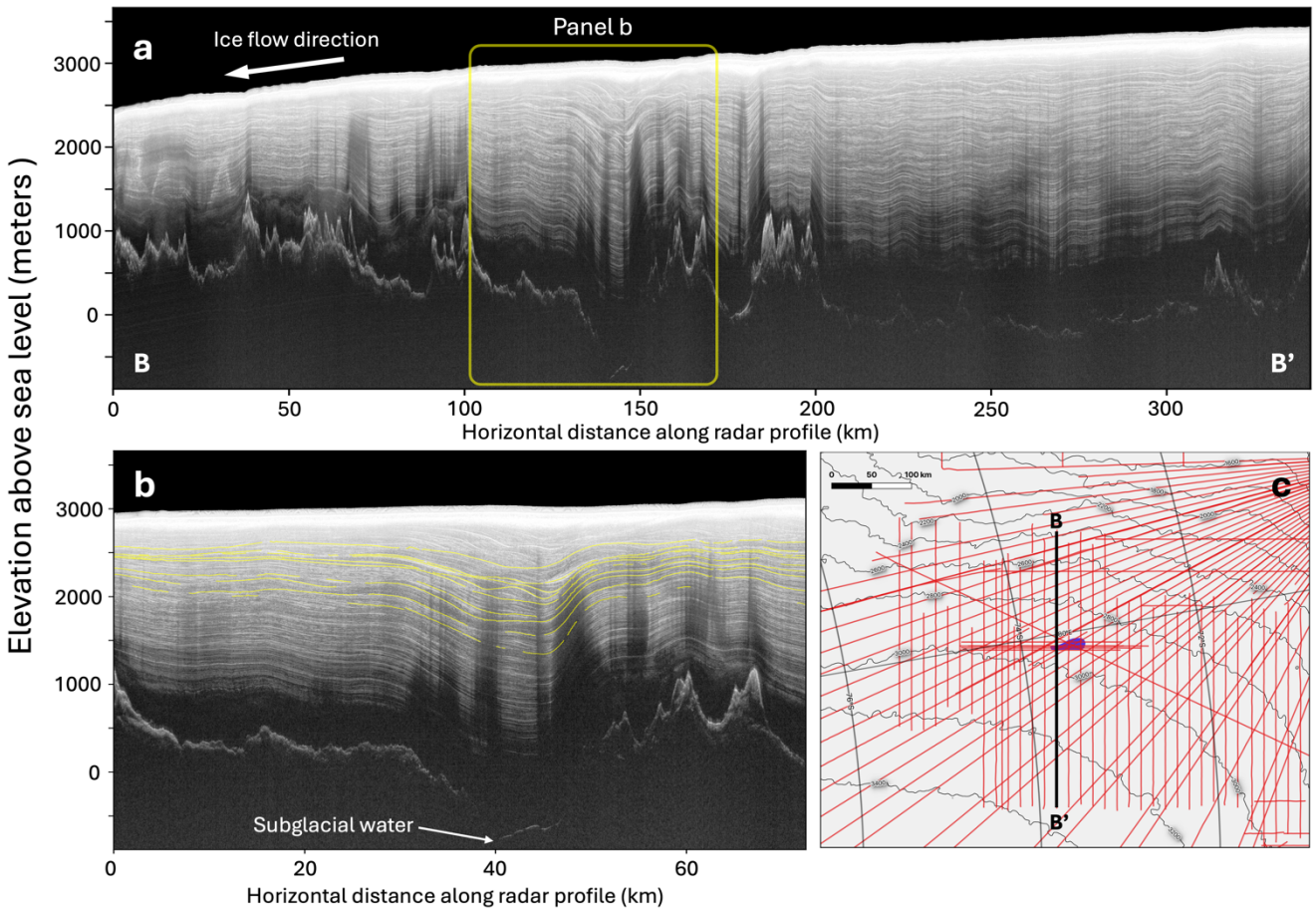

Fig. S2. Englacial radio-stratigraphy above LSE. a: Example radargram collected through the LSE area. The location and orientation of this radargram is marked in panel c. b: A zoom-in view of the anomalous stratigraphy above LSE, whose location is marked in panel a. Yellow lines show the nine traced englacial reflections in the LSE area, with PEL_EDC_IRH01 being the shallowest (closest to the ice surface) and PEL_EDC_IRH09 being the deepest. c: Location and orientation of the radargram shown in panel a with respect to LSE (blue area) and other survey profiles (red lines). Please note that this radargram is collected in the opposite orientation as the radargram shown in Fig. 2 and Fig. S1.

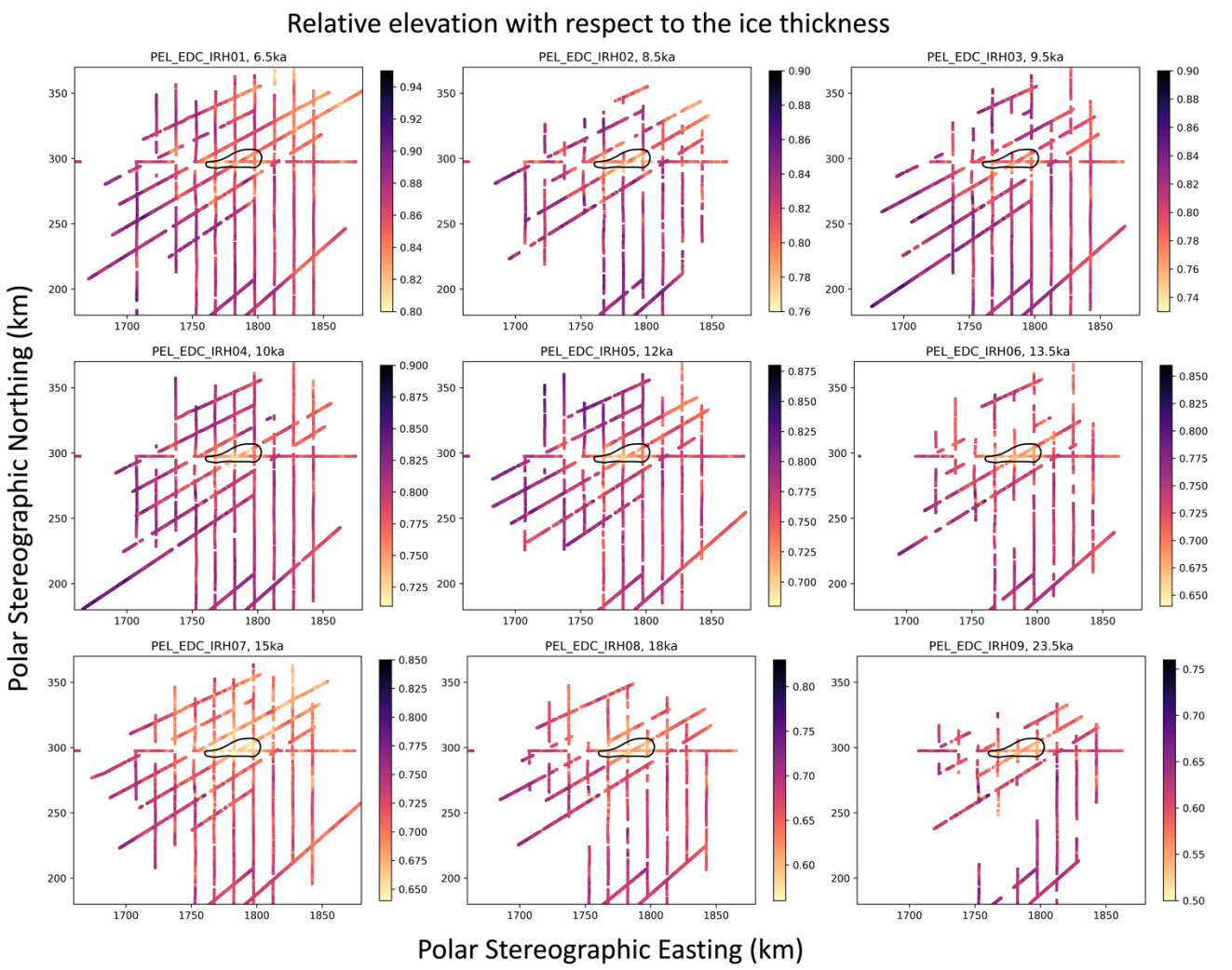

Fig. S3. Relative elevation of the nice traced IRHs, with respect to the ice sheet thickness.

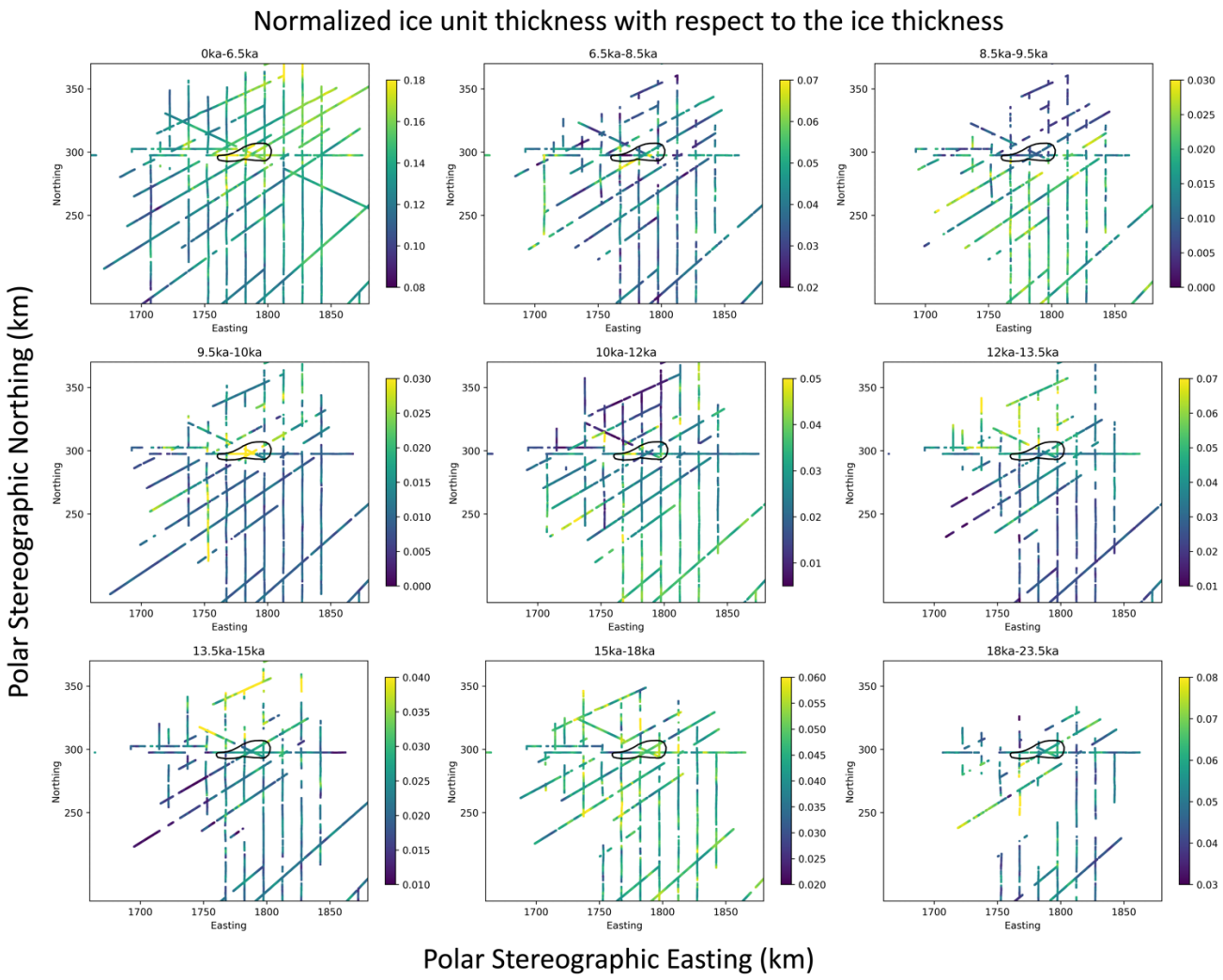

Fig. S4. Normalized thickness of ice units, with respect to the ice sheet thickness.

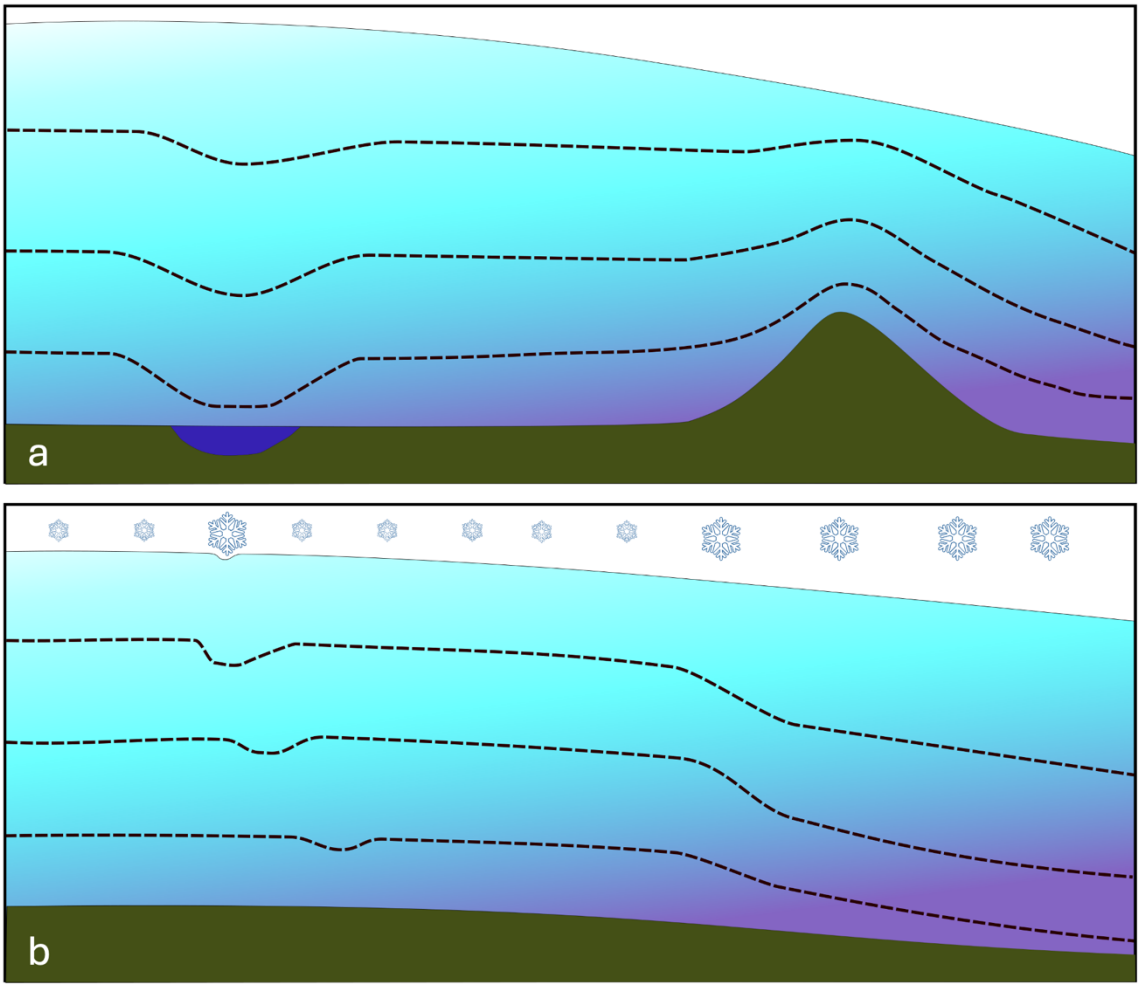

Fig. S5. Conceptual sketches showing the imprint on englacial stratigraphy of different processes. The ice sheet geometry is shown in blue, while the green area at the bottom represents the bedrock. a: The impact of changes in subglacial topography and basal melting. Deep blue area in the bedrock marks the location of a subglacial lake, where basal melting is present. b: The impact of variation in surface accumulation rate. The right half has a higher accumulation rate than the left. A localized increase of surface accumulation induced by local snow redistribution (resulting from an existing surface slope break) can be seen in the left half.

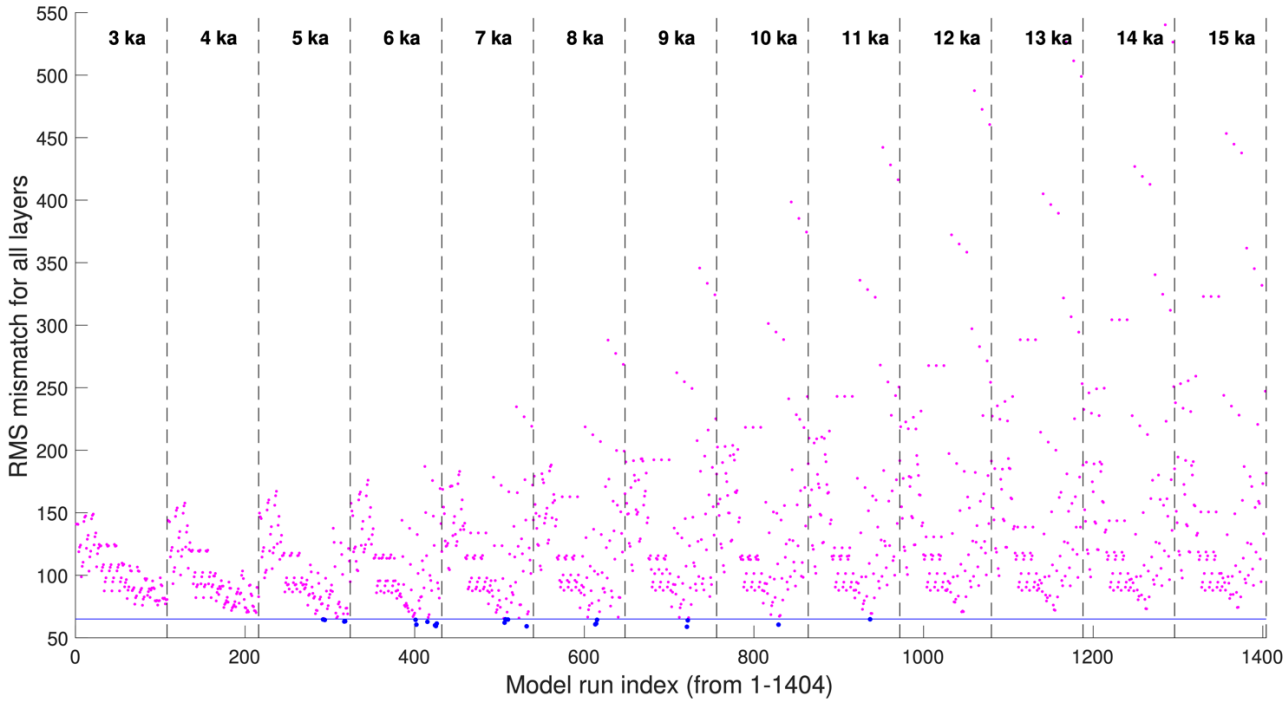

Fig. S6. RMS mismatch of all 1404 model setups, with mismatch smaller than the 65 meters threshold shown in bigger marker size. The time duration of the snowfall redistribution is noted on the top.

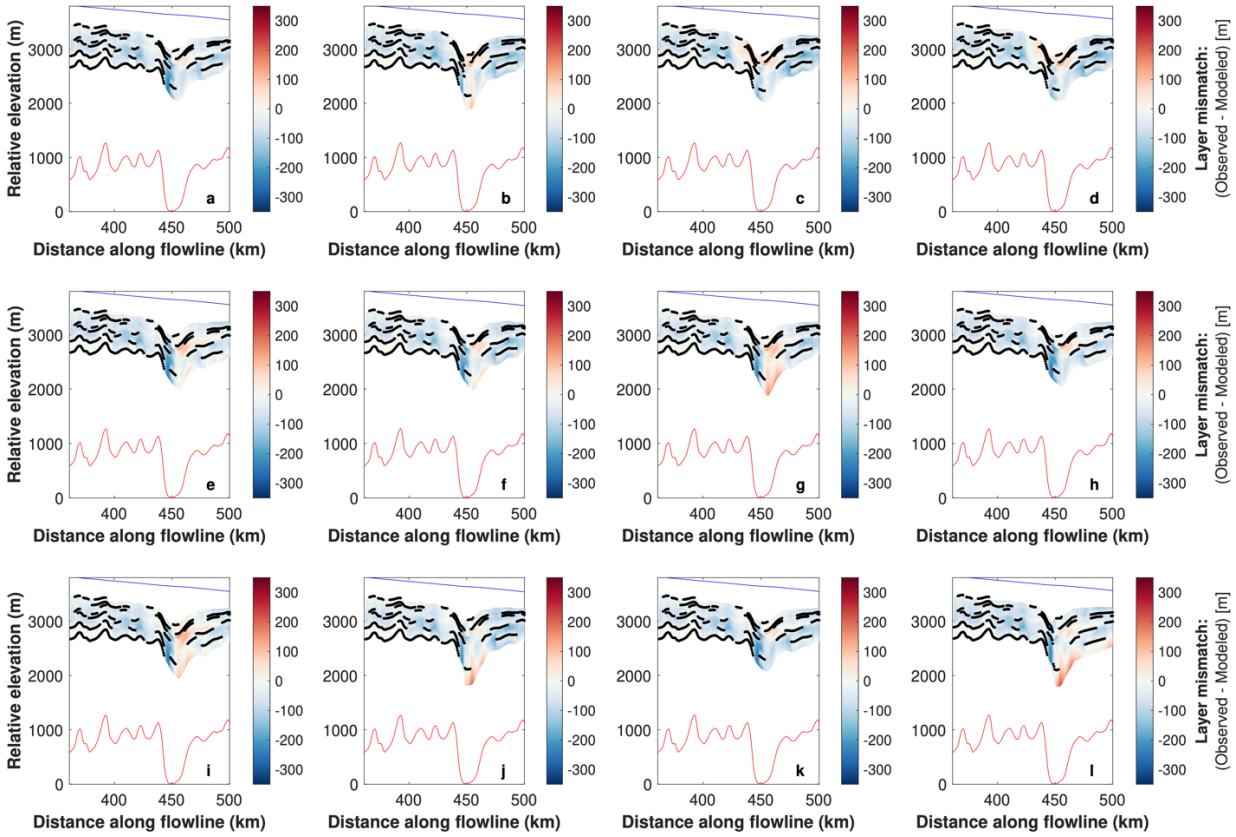

Fig. S7. Contour visualization of the accepted setups that are not shown in Figure 6 in the main text. The parameter combination for each setup is listed in Table S1.

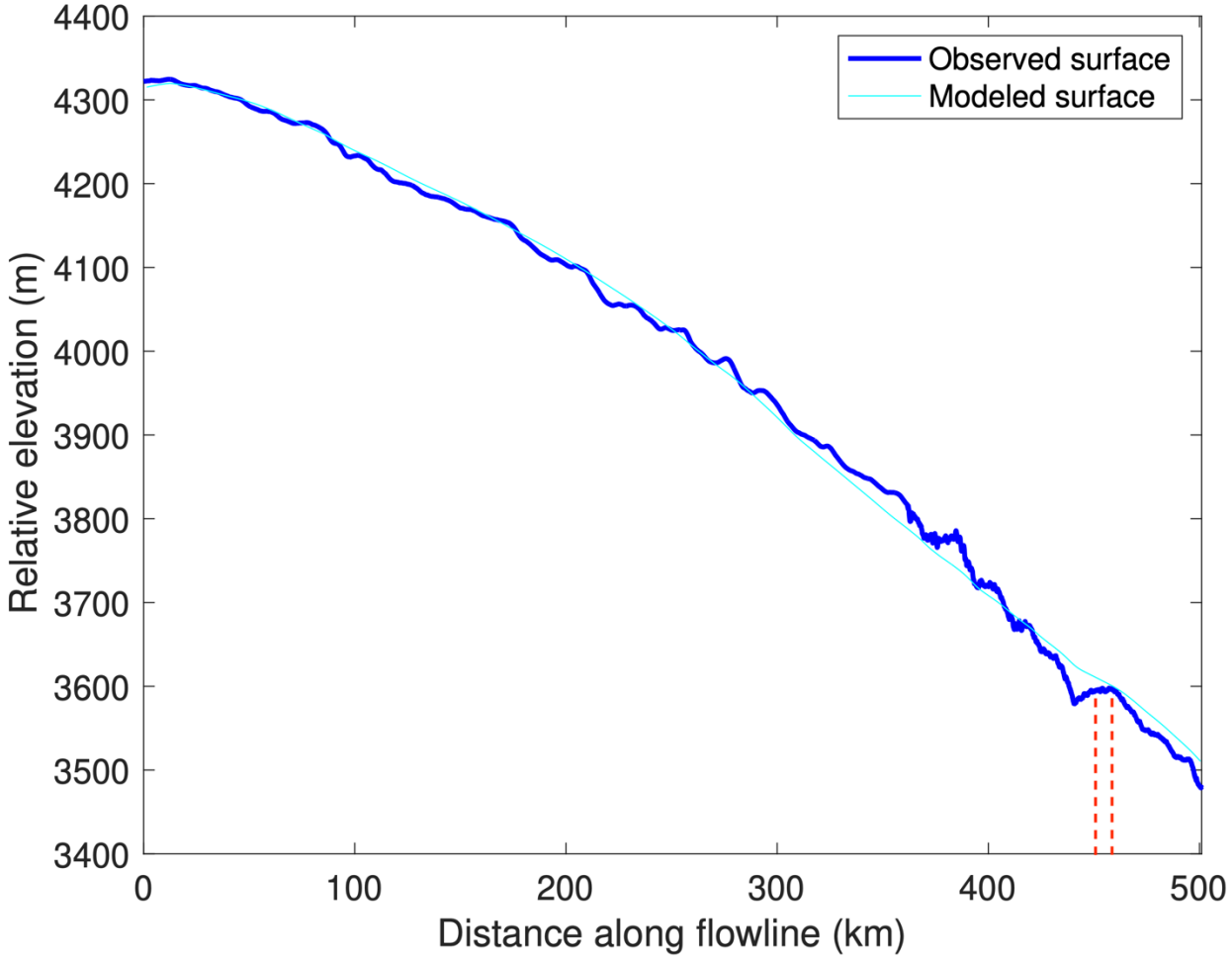

Fig. S8. Comparison between the measured surface elevation (Fretwell and others, 2013; Cui and others, 2020) and the modeled surface elevation along the model flowline. The location of LSE is marked with red dash line.

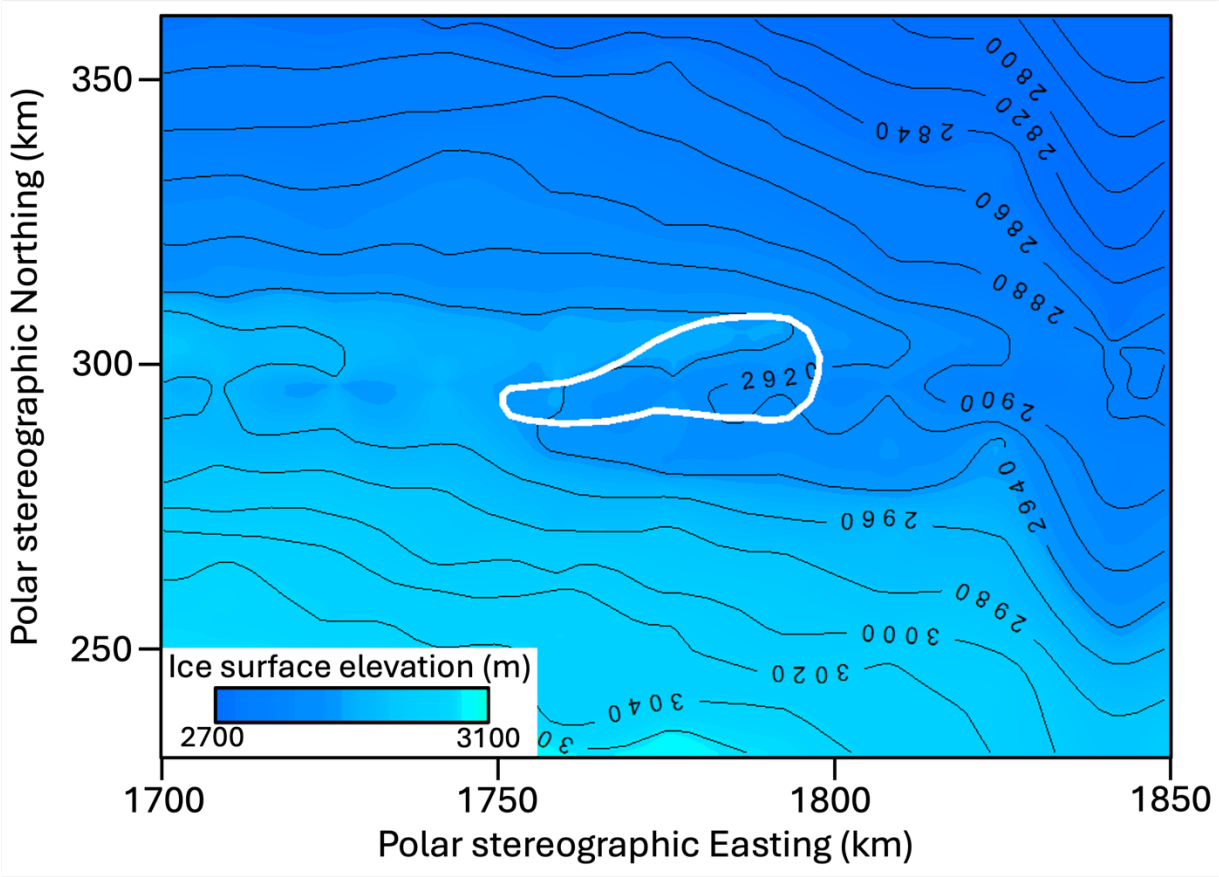

Fig. S9. Ice surface elevation map of the LSE area, adapted from Yan and others (2022). The shape and location of LSE is marked in white. This map shows the same area as Fig. 4.

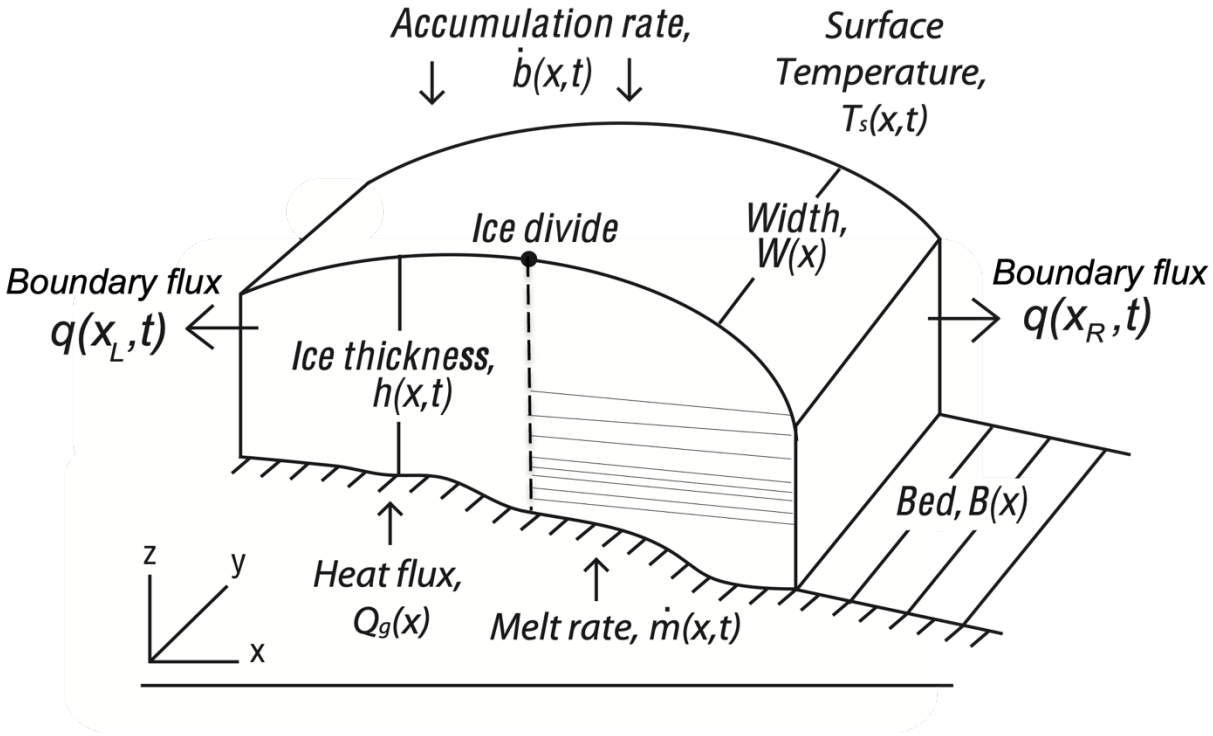

Fig. S10. A conceptual diagram illustrating the boundary conditions for the ice flow model, adapted from Koutnik and Waddington (2012).

Run index as shown in Fig. S7	Time duration of snowfall redistribution (kyr)	Surface accumulation increase percentage	Surface accumulation increase span (km)	Basal melt rate (m yr^{-1})	Plug flow velocity factor	Mismatch RMS (m)
a	7	150%	34	0.1	0.5	62
b	6	200%	24	0.1	0.1	63
c	5	200%	34	0.1	0.5	63
d	5	200%	34	0.1	0.7	63
e	9	150%	34	0.1	0.5	64
f	5	150%	34	0.2	0.7	64
g	6	150%	34	0.2	0.5	64
h	8	150%	34	0.1	0.7	64
i	7	150%	34	0.2	0.7	65
j	5	150%	34	0.2	0.1	65
k	7	150%	34	0.1	0.7	65
l	11	150%	34	0.1	0.1	65

Table S1. Parameters setup for the 12 runs with mismatch RMS values smaller than 65 meters that are not listed in Table 3. The mismatch contour produced by the model setups listed here are shown in Figure S7.

Reference:

Burton-Johnson A, Dziadek R and Martin C (2020) Review article: Geothermal heat flow in Antarctica: current and future directions. *The Cryosphere* **14**(11), 3843–3873. doi:10.5194/tc-14-3843-2020.

Cui X and others (2020) Bed topography of Princess Elizabeth Land in East Antarctica. *Earth System Science Data* **12**(4), 2765–2774. doi:10.5194/essd-12-2765-2020.

Fretwell P and others (2013) Bedmap2: Improved ice bed, surface and thickness datasets for Antarctica. *Cryosphere* **7**(1), 375–393. doi:10.5194/tc-7-375-2013.

Kang H, Zhao L, Wolovick M and Moore JC (2022) Evaluation of six geothermal heat flux maps for the Antarctic Lambert–Amery glacial system. *The Cryosphere* **16**(9), 3619–3633. doi:10.5194/tc-16-3619-2022.

Koutnik MR and Waddington ED (2012) Well-posed boundary conditions for limited-domain models of transient ice flow near an ice divide. *Journal of Glaciology* **58**(211), 1008–1020. doi:10.3189/2012JoG11J212.

Maule CF, Purucker ME, Olsen N and Mosegaard K (2005) Heat Flux Anomalies in Antarctica Revealed by Satellite Magnetic Data. *Science* **309**(5733), 464–467. doi:10.1126/science.1106888.

Rignot E, Mouginot J and Scheuchl B (2017) MEaSUREs InSAR-Based Antarctica Ice Velocity Map, Version 2. *Boulder, Colorado USA. NASA National Snow and Ice Data Center Distributed Active Archive Center*. doi:https://doi.org/10.5067/D7GK8F5J8M8R.

Yan S and others (2022) A newly discovered subglacial lake in East Antarctica likely hosts a valuable sedimentary record of ice and climate change. *Geology* **50(8)**, 949–953. doi:https://doi.org/10.1130/G50009.1.